Geochemistry, Geophysics, Geosystems®

RESEARCH ARTICLE
10.1029/2025GC012327

Contrasting Seismic Velocity and Compaction of Marine Calcareous Oozes and Volcaniclastic Deposits on the South Aegean Volcanic Arc

M. Manga[1], V. Wright[2], T. Cadena[1], I. McIntosh[3], J. Preine[4,5], M. Tominaga[4], P. Nomikou[6], T. Druitt[7], S. Kutterolf[8], S. Beethe[9], T. A. Ronge[10], C. Hübscher[5], J. Karstens[8], G. Kletetschka[11,12], Y. Yamamoto[13], A. Woodhouse[14,15,16], R. Gertisser[17], A. Peccia[18], A. Clark[19], and IODP Expedition 398 Participants[20]

[1]Department of Earth and Planetary Science, University of California, Berkeley, CA, USA, [2]Scripps Institution of Oceanography, University of California, San Diego, CA, USA, [3]Institute of Marine Geodynamics, Japan Agency for Marine Earth Science and Technology, Yokosuka, Japan, [4]Department of Geology and Geophysics, Woods Hole Oceanographic Institution, Woods Hole, MA, USA, [5]Institute of Geophysics, University of Hamburg, Hamburg, Germany, [6]Department of Geology and Geoenvironment, National and Kapodistrian University of Athens, Athens, Greece, [7]Laboratoire Magmas et Volcans, Université Clermont-Auvergne, CNRS, IRD, OPGC, Clermont-Ferrand, France, [8]GEOMAR Helmholtz Centre for Ocean Research Kiel, Kiel, Germany, [9]College of Earth Ocean and Atmospheric Sciences, Oregon State University, Corvallis, OR, USA, [10]Scientific Ocean Drilling, Texas A&M University, College Station, TX, USA, [11]Faculty of Science, Institute of Hydrogeology, Engineering Geology and Applied Geophysics, Charles University, Prague, Czech Republic, [12]Geophysical Institute, University of Alaska, Fairbanks, AK, USA, [13]Graduate School of Science, Kobe University, Kobe, Japan, [14]School of Earth and Environmental Sciences, Cardiff University, Cardiff, UK, [15]School of Earth Sciences, University of Bristol, Bristol, UK, [16]University of Texas Institute for Geophysics, University of Texas at Austin, Austin, TX, USA, [17]School of Life Sciences, Keele University, Keele, UK, [18]Lamont-Doherty Earth Observatory, Columbia University, Palisades, NY, USA, [19]CODES, School of Natural Sciences, University of Tasmania, Hobart, TAS, Australia, [20]Affiliations listed in supplement

Abstract International Ocean Discovery Program Expedition 398 recovered more than 2,200 m of volcaniclastic deposits from 12 sites and 28 holes from Santorini Caldera, Greece, and the surrounding rift basins in the South Aegean Volcanic Arc. We compare and contrast discrete shipboard measurements of physical properties (density, P-wave velocity) of these volcaniclastic sediments with other uncemented marine sediments in the cores. The grain density (mass of solids divided by their volume, including any isolated vesicles) of volcaniclastic deposits is typically lower than that of volcanic glass and crystals and is sometimes less than 2 g/cm^3, indicating the preservation of isolated gas-filled vesicles in erupted materials. Volcaniclastic deposits typically have higher P-wave velocities but lower bulk densities than oozes and other marine sediments. In volcaniclastic deposits, lapilli have higher P-wave velocities and lower bulk density than ash, the opposite trend of most sediment in which higher density is correlated with higher seismic velocity. We use granular physics models to show that the higher volcaniclastic P-wave velocity originates from two effects: (a) lower pore volume outside clasts that increases elastic moduli and (b) isolated gas vesicles in volcanic clasts that lower bulk density. In volcaniclastic sediments there is relatively little change in physical properties to depths of several hundred meters below the seafloor, which we attribute to rough grain surfaces and lower intergranular (external) porosities that hinder compaction and the decrease of intergranular pore space. These trends lead to distinctive signatures of volcaniclastic sediments in reflection seismic images.

Plain Language Summary The density and seismic velocity of marine sediments, and how they vary with depth, depend on the properties of the sediment, including their composition and the sizes and shapes of particles. International Ocean Discovery Program Expedition 398 recovered volcanic and non-volcanic sediment from the South Aegean Volcanic Arc in the Mediterranean Sea. Shipboard measurements on these samples enable us to understand some of the controls on sediment density and seismic velocity. Deposits of particles with volcanic origins have higher seismic velocities than other marine sediments, despite having lower densities. The low density arises in part because volcanic particles contain vesicles that are filled with water and gas. The higher seismic velocity is due to smaller amounts of pore space around the volcanic particles in addition to the trapped gas (bubbles) inside the particles.

Key Points:

- In volcaniclastic deposits, lapilli have higher P-wave velocities and lower bulk density than ash
- Isolated gas-filled vesicles in volcanic clasts lead to lower bulk density than other sediments
- Volcaniclastic deposits compact less than calcareous oozes with respect to depth

Supporting Information:

Supporting Information may be found in the online version of this article.

Correspondence to:

M. Manga,
mmanga@berkeley.edu

Citation:

Manga, M., Wright, V., Cadena, T., McIntosh, I., Preine, J., Tominaga, M., et al. (2025). Contrasting seismic velocity and compaction of marine calcareous oozes and volcaniclastic deposits on the South Aegean Volcanic Arc. *Geochemistry, Geophysics, Geosystems*, *26*, e2025GC012327. https://doi.org/10.1029/2025GC012327

Received 19 MAR 2025
Accepted 3 SEP 2025

Author Contributions:

Conceptualization: M. Manga, V. Wright
Data curation: T. Cadena
Formal analysis: M. Manga, V. Wright, T. Cadena, I. McIntosh
Funding acquisition: M. Manga, T. Druitt, S. Kutterolf, T. A. Ronge
Investigation: M. Manga, V. Wright, T. Cadena, I. McIntosh, J. Preine, M. Tominaga, P. Nomikou, T. Druitt, S. Kutterolf, S. Beethe, T. A. Ronge, C. Hübscher, J. Karstens, G. Kletetschka, Y. Yamamoto, A. Woodhouse, R. Gertisser, A. Peccia, A. Clark
Methodology: M. Manga, V. Wright

Project administration: M. Manga, T. Druitt, S. Kutterolf, T. A. Ronge
Resources: M. Manga
Software: M. Manga, V. Wright
Supervision: M. Manga, T. Druitt, S. Kutterolf, T. A. Ronge
Validation: V. Wright
Visualization: M. Manga, T. Cadena, J. Preine
Writing – original draft: M. Manga, V. Wright
Writing – review & editing: M. Manga, V. Wright, T. Cadena, J. Preine, T. Druitt, S. Kutterolf, T. A. Ronge, C. Hübscher, R. Gertisser

Densities and seismic velocities of volcanic particles increase more slowly with increasing depth than other marine sediments. Together, the measurements and trends help guide the interpretation of seismic images of seafloor deposits.

1. Introduction

Volcaniclastic sediments are deposited on the submarine flanks of arc volcanoes and in adjacent basins, and individual volcanic eruptions can create deposits tens to hundreds of meters thick (Cas & Wright, 1991; Metcalfe, Druitt, Pank, Kutterolf, Preine, Kelfoun et al., 2025; Shimizu et al., 2024). Deposition can occur as subaerial fall deposits sediment through the water column (Cashman & Fiske, 1991; Freundt et al., 2023), as clasts in floating rafts saturate and then sink (Fauria et al., 2017; Jutzeler et al., 2017), or from submarine density currents (Clare et al., 2023; Druitt, Kutterolf, Ronge, Hübscher, et al., 2024). While volcaniclastic sediments are a small fraction of the global marine sediment budget (Dutkiewicz et al., 2015; Straub & Schmincke, 1998), they can locally comprise a large fraction of the volume of sediment near submarine and ocean-adjacent volcanic arcs. Despite their local and regional importance for physical, hydrothermal, chemical, and biological processes (Carey et al., 2025), there are few settings where we have a comprehensive set of physical properties measurements on marine sediment of volcanic origin. Some examples include data from International Ocean Discovery Program (IODP) Expeditions, including Expedition 340 to the Lesser Antilles Arc (Le Friant et al., 2015), Expedition 350 to the Izu-Bonin-Mariana Rear Arc (Busby et al., 2017), Expedition 351 to the Izu-Bonin-Mariana arc (Arculus et al., 2015), Expedition 352 to the Izu-Bonin Arc (Kutterolf et al., 2018), Expedition 322 to the Nankai Trough (Underwood et al., 2010), and Ocean Drilling Program Site 1,149 east of the Izu-Bonin trench (Scudder et al., 2009).

Physical property measurements can help identify volcaniclastic deposits in geophysical data sets, if physical properties of sediments with volcanic and non-volcanic origins are different and can be recognized. Thus, these measurements help to determine eruption style and transport processes, along with erupted bulk volumes and masses (Cassidy et al., 2014; Hanyu et al., 2024; Hübscher et al., 2015; Karstens et al., 2023; Manville et al., 2009; Portner et al., 2015). Densities of volcanic sediments are different from most non-volcanic sediments because the volcanic particles can contain internal pore space, some of which may be filled with gas if the vesicles are fully isolated by being completely surrounded by quenched glass. Thus, relationships between bulk sediment density and other physical properties can be fundamentally different for marine volcanic sediment compared with most other marine sediment.

A new opportunity to measure and understand the physical properties of marine volcanic sediments was provided through IODP Expedition 398, which aimed to unravel the history of the Christiana-Santorini-Kolumbo Volcanic Field (CSKVF) in the South Aegean Volcanic Arc (Druitt, Kutterolf, Ronge, Beethe, et al., 2024a). Volcanic sediments recovered during IODP Expedition 398 represent 30% of the total drilled length of all holes combined (7.3 km), 66% of the recovered sediments, and 33% of the discrete layers identified within the recovered sediments (Druitt, Kutterolf, Ronge, Beethe, et al., 2024a). Physical properties, including compressional wave velocity (P-wave velocity, V_p), bulk (ρ_b) and grain (ρ_g) density, magnetic susceptibility, thermal conductivity, and shear strength, were measured on drilled and recovered cores on the ship during the expedition. The primary objectives of the physical properties program on this expedition were to collect high-resolution physical properties data on cored materials that (a) identify major volcaniclastic deposits and mass transport events, (b) constrain geothermal, geomechanical, and seismic properties of the deposits, (c) construct composite stratigraphic correlations and eruption chronologies, and (d) create synthetic seismograms to assist core-seismic integration (Preine et al., 2025). In addition, physical properties measurements provide data that assist in the characterization of lithological units, heat flow, fluid flow, consolidation, and basin subsidence history. They also help with interpreting downhole geophysical logging data.

Compaction and loss of pore space with increasing burial depth occur primarily because of mechanical compaction and pressure solution. Collectively, these processes lead to an approximately exponential decrease of porosity with increasing burial depth captured by Athy's law (Athy, 1930) though porosity is primarily determined by effective stress rather than depth (Bredehoeft & Hanshaw, 1968; Dickinson, 1953; Shi & Wang, 1986). Lithology matters too. For example, mechanical compaction from particle slippage and rotation is sensitive to particle shape (Terzaghi & Peck, 1948). Thus, for example, clay-rich sediments compact more rapidly with

increasing effective stress (and depth) than coarser siliciclastic sediments (Revil et al., 2002). IODP Expedition 398 thus also provided a new opportunity to study compaction (consolidation) of volcaniclastic sediments at shallow depths and compare and contrast volcaniclastic sediment with other marine sediments.

Here, we compare and contrast the physical properties of uncemented sediment of volcanic and non-volcanic origin recovered from similar depth intervals. We focus on V_p and bulk density because these two physical properties inform the interpretation and use of seismic survey data. Seismic profiles in the region offer much broader spatial coverage than the small number of deep holes cored by IODP Expedition 398. In particular, in this study we consider where and why bulk density and V_p differ between volcanic and non-volcanic sediment and how these quantities vary with depth.

2. Setting

Oceanic and submarine volcanoes are the most active and widespread volcanoes on Earth. Much of the erupted materials from these volcanoes accumulate in the sedimentary basins surrounding the volcanoes or within submarine calderas. The record preserved subaerially on islands may record only the subset of eruption phenomena that enable on-land deposition and are subject to erosion through rain and wind (Druitt, Kutterolf, Ronge, Hübscher, et al., 2024; Preine et al., 2024). The volcanic centers in the South Aegean Volcanic Arc in the Aegean Sea are examples where most of the erupted material is deposited offshore, and many of the eruptions were submarine. South Aegean Volcanic Arc eruptions include the 35 km^3 (dense rock equivalent, DRE) iconic 3.6 ka Late Bronze Age eruption that formed the present caldera of Santorini (Karstens et al., 2023) and the more recent 1650 CE 2 km^3 DRE submarine eruption of Kolumbo that killed 70 people on Santorini (Cantner et al., 2014; Fuller et al., 2018). A dense network of seismic profiles has been collected in this region to map volcanic deposits and decipher the relationship between volcanism and regional tectonics (Hübscher et al., 2015; Johnston et al., 2015; Nomikou et al., 2013, 2016, 2018; Preine, Hübscher, et al., 2022; Sigurdsson et al., 2006). IODP Expedition 398 between 11 December 2022 and 10 February 2023 included ground-truthing those seismic profiles to better determine the volume, dispersal, and history of large eruptions and flank collapse events of the CSKVF in the South Aegean Volcanic Arc (Druitt, Kutterolf, Ronge, Beethe, et al., 2024a).

The CSKVF has evolved since the Pliocene with the formation of the Christiana volcano, which became inactive around 1.6 Ma (Heath et al., 2019; Piper et al., 2007; Preine, Hübscher, et al., 2022). In the Middle Pleistocene, the Archaeos Tuff eruption deposited at least 89 km^3 of tephra in the surrounding basins (Druitt, Kutterolf, Ronge, Hübscher, et al., 2024). A major change in volcanic activity occurred around 250 ka, when volcanism became highly explosive (Metcalfe, Druitt, Pank, Kutterolf, Preine, Kelfoun, et al., 2025; Metcalfe, Druitt, Pank, Kutterolf, Preine, Beethe, et al., 2025). The products of this phase are known as the Thera Pyroclastic Formation and are mostly found on the caldera cliffs of Santorini volcano (Druitt et al., 1999). Offshore, these deposits form a thick wedge north of Santorini, and represent significant volcanic megabeds in the Anhydros and Anafi Basins (Metcalfe, Druitt, Pank, Kutterolf, Preine, Beethe, et al., 2025; Preine, Hübscher, et al., 2022; Preine, Karstens, et al., 2022).

Figure 1 shows the locations of 12 sites cored during IODP Expedition 398. Sites U1594-U1597 are located within the Santorini caldera and cored materials that postdate the 3.6 ka Late Bronze Age eruption that formed the caldera. The remaining sites sampled deposits within the rift basins hosting the CSKVF.

3. Methods

Physical properties were measured on the JOIDES Resolution following standard IODP procedures. Measurement methods are described in detail in Kutterolf et al. (2024), and here we provide a brief summary of relevant measurement procedures for interpreting the results we present. Bulk density, magnetic susceptibility, and P-wave velocity are measured continuously at 2.5 cm intervals on whole-round cores after equilibrating to the laboratory temperature on the ship. Despite the high spatial resolution of these measurements, we do not use or interpret these data in the present study, except for comparison with seismic images. These measurements can be impacted by cracks and partially filled core-liners, and V_p was sometimes difficult to measure on whole cores due to coarse volcaniclastic materials. Instead, we rely on discrete measurements made where shipboard scientists could assess the cores for disturbances. After the cores were split into working and archive halves, physical samples were collected for moisture and density (MAD) measurements, and discrete measurements of V_p were

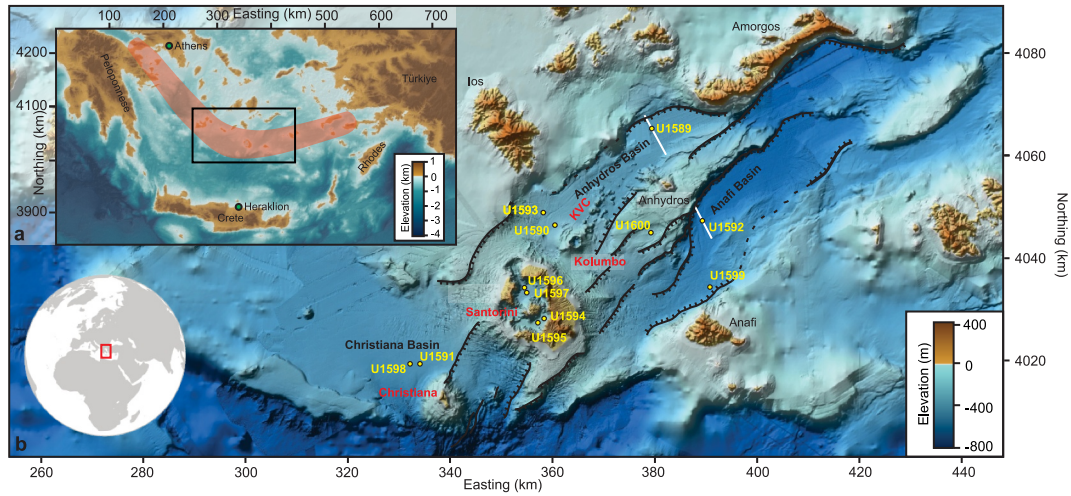

Figure 1. Location of sites drilled and cored during International Ocean Discovery Program Expedition 398 to the South Aegean Volcanic Arc and the Christiana-Santorini-Kolumbo Volcanic Field. Sites U1594–U1597 are located within the Santorini Caldera formed by the 3.6 ka Late Bronze Age eruption. White lines indicate seismic reflection profiles shown in Figures 9c and 9f.

obtained, typically about one sample or measurement per 1.5 m long core section. We view these data as more reliable and of better quality than the whole-round data, and these are the data we interpret here, though all data are available at Druitt, Kutterolf, Ronge, et al. (2024). Further descriptions of instruments, quality control and core analysis workflow are provided in Kutterolf et al. (2024).

Downhole logging to obtain in situ physical property measurements was initially planned for all sites. However, drilling in unconsolidated volcaniclastic sediment proved challenging because the holes were unstable and prone to collapse (Druitt, Kutterolf, Ronge, Beethe, et al., 2024a). Logging was, thus, only performed in Hole U1589C.

3.1. Moisture and Density (MAD) Measurements

Water content, bulk density, grain density, and porosity are determined most accurately by measuring mass and volume on discrete samples. The shipboard MAD facility on the JOIDES Resolution includes a helium pycnometer and a dual balance system to account for the motion of the ship (Kutterolf et al., 2024).

Sediment volumes of $\sim$6 cm^3 were extracted from the working half of the core while they remained fully saturated. The wet sample mass was measured immediately after sampling. Dry sample mass and volume were measured after drying the samples in a convection oven for 24 hr at a temperature of 105° $\pm$ 5°C and then cooling them within a desiccator for 3 hr. Dry volume was measured using a helium-displacement pycnometer. Volumes are averaged over three measurements. Traditional IODP methods are used to calculate sediment bulk density (ρ_b, water-saturated sediment density), dry density (all pore water evaporated), grain density (ρ_g, mass of sediment particles divided by their volume that includes isolated vesicles), and porosity (percentage of sediment i.e., filled with water that can evaporate), with a correction for salt dissolved in pore water (Blum, 1997). These different types of pore spaces are illustrated in Figure 2. Because volcanic clasts can contain large intragranular porosity, we refer to the pore space inside clasts as internal porosity and distinguish between connected intragranular pores that fill with water from isolated porosity that remains gas-filled. The intergranular pore space is referred to as external porosity to distinguish it from the two types of internal porosity. Corrections for salt assumed a pore water salinity of 0.035 per mil (Kutterolf et al., 2024).

3.2. P-Wave Velocity

The measurement of V_p was carried out on wet sediment in the working half of the split cores using the P-wave gantry system. We report measurements made perpendicular to the core. To ensure good contact between the transducers and sediment, deionized water was applied to the lower transducer, which was in contact with the core liner. Plastic film was placed on the split core surface to protect the upper transducer.

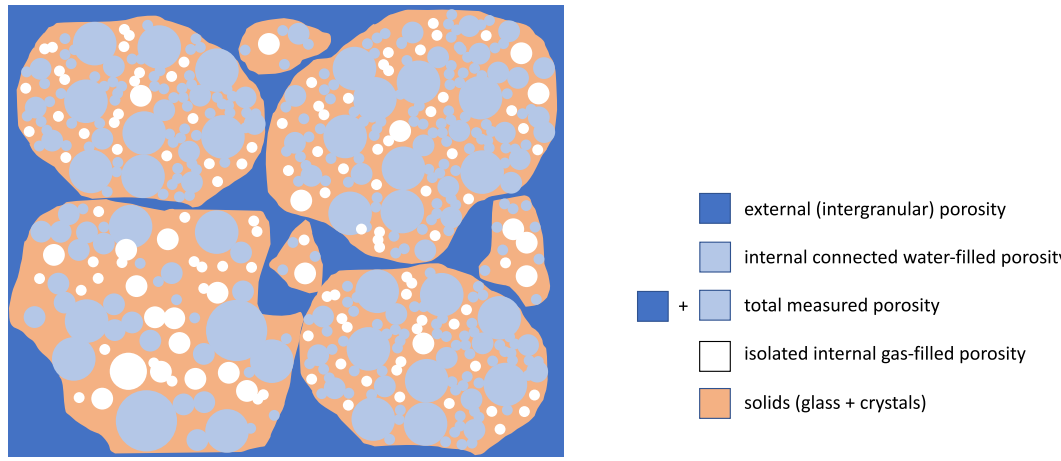

Figure 2. Illustration of the types of pore spaces in volcaniclastic sediment.

The system uses Panametrics-NDT Microscan delay line transducers with a frequency of 500 kHz. The distance between the two transducers was measured with a built-in linear variable differential transformer. Measurements account for the core liner thickness.

3.3. Downhole Logging

Hole U1589C was logged using the triple-combination tool string equipped with natural gamma radiation (Hostile Environment Natural Gamma Ray Sonde), litho-density (Hostile Environment Litho-Density Sonde), electrical resistivity (High-Resolution Laterolog Array), and magnetic susceptibility (Magnetic Susceptibility Sonde) sensors. Details of operations, deployment, and measurements are provided in Druitt, Kutterolf, Ronge, Beethe, et al. (2024b).

3.4. X-Ray Computed Microtomography Imaging

X-ray computed microtomography (μXRT) enables three-dimensional imaging of the internal structure of the clasts by measuring the absorption of X-rays for each component (solids, water, gas) comprising the multiphase sample. Pumice clasts were picked from specific units of interest for shore-based studies of their textures. Those clasts were saturated with water under vacuum for 24 hr and subsequently stored in water. We selected a pumice clast from site U1591A and section 9H-1-W for imaging, 15 months after immersion in water. This clast comes from the mid-Pleistocene Archaeos Tuff (Druitt, Kutterolf, Ronge, Hübscher, et al., 2024). Imaging was performed with μXRT at the Advanced Light Source on beamline 8.3.2 using 28 keV monochromatic X-rays. Tomographic reconstructions are based on 1,969 images collected over 180 degrees of rotation with a 10x lens, enabling a voxel linear dimension of 0.635 μm. The lowest density regions absorb the least X-rays and therefore appear as the lowest intensity pixels (darkest) in the original grayscale tomography image: these regions correspond to the isolated vesicles. The highest intensity (brightest) regions correspond to the glass and crystals, and the intermediate intensity regions correspond to the water-filled vesicles. Pre-processing, segmentation, and visualization were achieved using Dragonfly 3D World 2024.1 software under an annual license agreement (Comet Technologies Canada Inc, 2024). Raw images were pre-processed using intensity normalization and a 3D median smoothing filter. Multiphase segmentation of a sub-volume of the imaged clast was performed with the Dragonfly Segmentation Wizard. A portion of a tomography image was painted using the Region of Interest (ROI) tools to tag pixels corresponding to three classes (solids, water, and gas), providing sparse training data for a U-Net convolutional neural network image segmentation model. The initial guess of the model was loaded onto the entire image (training frame) and ROI tools were used again to correct and refine the model output. This process was repeated for several frames spanning the sub-volume, then all precisely tagged frames were used for training and validation of the final U-Net model. This model was applied to the entire sub-volume image stack and produced a multi-Region of Interest (multi-ROI) comprised of segmented solids, water, and gas. The multi-ROI was then made into a 3D mesh, smoothed, and colored for optimal visualization.

3.5. Granular and Rock Physics Models

In the discussion, we use theoretical models that predict V_p as a function of sediment properties to interpret means, trends, and differences between our measurements. Hashin-Shtrikman-Walpole bounds (Hashin & Shtrikman, 1963; Walpole, 1966) are used to determine the elastic moduli of clasts and whether they contain water- and gas-filled vesicles. Because the sediments are unconsolidated, owing to a combination of low temperatures (Manga et al., 2025), Pleistocene ages (Druitt, Kutterolf, Ronge, Beethe, et al., 2024a), and depths less than a few hundred meters (Fowler & Yang, 1999), granular physics models are used to determine bulk sediment properties from the properties of clasts. Details of the models are summarized in Appendix A and the codes used to compute model predictions are provided at Wright and Manga (2025).

4. Results

Because physical properties were measured on recovered cores and hence might be impacted by coring and recovery, we first assess whether the measurements are representative of in situ conditions by comparing bulk density measurements with downhole in situ logging data from site U1589 where logging was undertaken. We compare and contrast measurements on volcaniclastic materials from the caldera to assess differences between lapilli and ash size fractions. We then compare how physical properties vary with depth in the sedimentary basins and, in particular, the difference between volcaniclastic sediment and calcareous oozes. As the dominant component of the recovered oozes was calcareous nannofossils, we hereafter refer to it simply as "ooze" for brevity. MAD measurements and V_p were not measured on the same samples–the MAD samples were extracted after the core was split and before V_p was measured. We thus do not plot V_p versus MAD data and instead interpret trends with depth and means. We plot our measurements as a function of depth, rather than pressure, as the former is the directly measured quantity and we have no in situ stress measurements. Compaction, however, is largely driven by lithostatic overburden over the ages and depths sampled by our cores (Fowler & Yang, 1999; Weller, 1959). Pressure enters in the rock physics models in Equations A3 and A4, thus, for the calculations we convert depth to pressure.

4.1. Comparison of Downhole Logging and Shipboard Measurements

Figure 3 compares in situ logging measurements of formation density in Hole U1589C with discrete bulk density measurements on the materials recovered from Holes U1589A and U1589B. We undertake this comparison with the premise that logging measures properties in situ, and this to be a basis of assessing our shipboard measurements where sampled materials may have been impacted by coring and recovery. We exclude measurements from depths with reported coring disturbances (Jutzeler et al., 2025). In general, the agreement for oozes is good, even capturing the downhole variations in density, though we emphasize that logging and discrete measurements were conducted in different holes. Further, the logging data measure and average over a larger volume than the $\sim$6 cm^3 of our shipboard samples; the investigation depth of the Hostile Environment Litho-Density Sonde is tens of centimeters and the vertical resolution is 38 cm (https://iodp.tamu.edu/tools/logging/TRIPLE/hlds.html).

The shipboard bulk density of the 16 ooze samples over the depth interval with logging data is 1.87 $\pm$ 0.10 g/cm^3; the mean of the logging data at the same depths is 1.84 $\pm$ 0.11 g/cm^3. There are only six ash samples in the logged interval, with a mean bulk density of 1.68 g/cm^3 compared with a logging density of 1.83 g/cm^3, and logging and shipboard measurements show large variability. Some of the density decrease could arise from stress release as samples are brought to the surface. If there was any intergranular pore water drainage, this would lower the shipboard measured bulk density, though we have no visual evidence for drainage. Overall, comparing shipboard discrete density measurements and logging data suggests that shipboard measurements provide reasonable estimates of in situ conditions.

4.2. Caldera Sites

Sites U1594–U1597 within Santorini Caldera cored almost exclusively volcaniclastic materials, much of which came from a 726 CE post-caldera eruption of Kameni (Preine et al., 2024). Given the limited lithologies and young ages compared to other sites, we analyze these deposits separately from sites outside the caldera. In particular, we use the caldera sites to compare and contrast the densities and seismic velocities of ash compared to lapilli (with standard definition of 2 mm separating ash and lapilli (Fisher, 1961), and identified during core description on the ship).

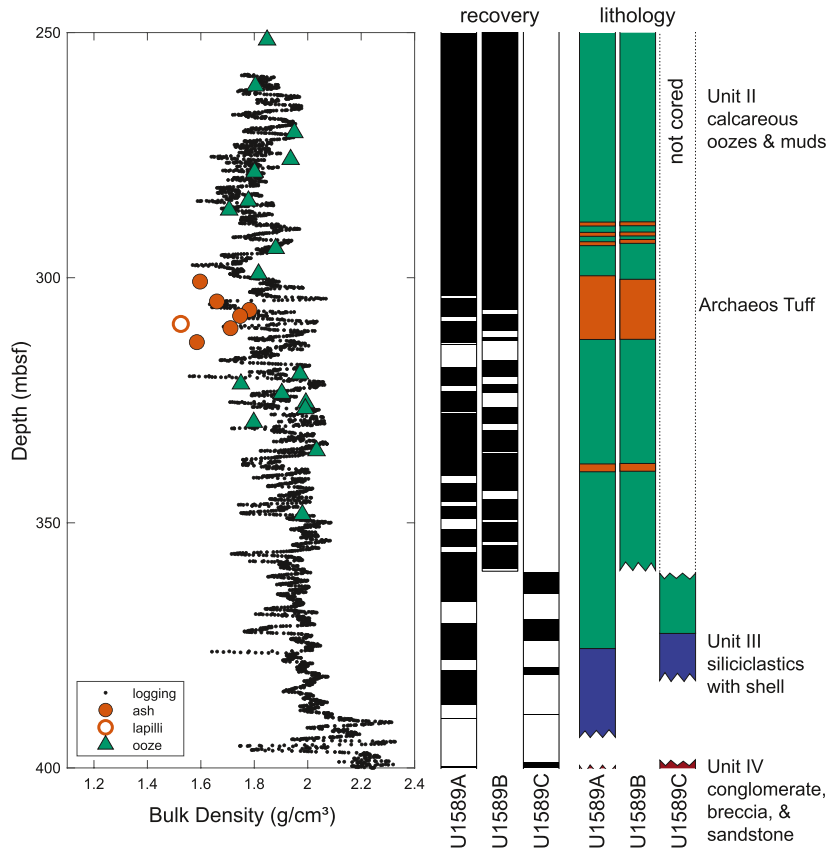

Figure 3. Comparison of logging and shipboard data. Shipboard measurements were made on cores from U1589A and U1589B; logging was performed in U1589C. Triangles indicate ooze data, and circles indicate volcaniclastic data. In the recovery column, black indicates the depth from which cores were successfully recovered. Green indicates oozes in the lithology column, and orange indicates volcaniclastic units. Depth is the CSF-A scale. The depth interval from 300 to 308 m is the Archaeos Tuff (Druitt, Kutterolf, Ronge, Hübscher, et al., 2024).

Table 1 summarizes discrete measurements of bulk density, porosity, grain density, and P-wave velocity. Lapilli have lower bulk and grain densities than ash but higher V_p. Porosities (sum of external and connected water-filled internal porosities, as defined in Figure 2) are similar and overlap within much less than one standard deviation. In contrast, the differences in bulk density, grain density, and P-wave velocity between ash and lapilli are greater than the standard deviation of any one of the measurements.

4.3. Sedimentary Basin Sites

Figure 4 shows depth variations of porosity, bulk density, grain density, and P-wave velocity for lithologies identified on the ship as calcareous ooze, volcanic lapilli, and volcanic ash. Mixed lithologies such as those described as tuffaceous ooze are omitted. In typical marine sediment, porosity decreases approximately

Table 1
Physical Properties From Santorini Caldera Sites U1594–U1597

Material	Bulk density (g/cm^3)	Porosity (%)	Grain density (g/cm^3)	P-wave velocity (m/s)
ash	1.588 ± 0.161	61.1 ± 8.2	2.457 ± 0.142	1623.0 ± 81.6
	n = 30			n = 304
lapilli	1.357 ± 0.119	63.4 ± 7.0	1.932 ± 0.220	1869.5 ± 181.5
	n = 32			n = 181

Note. ± shows one standard deviation.

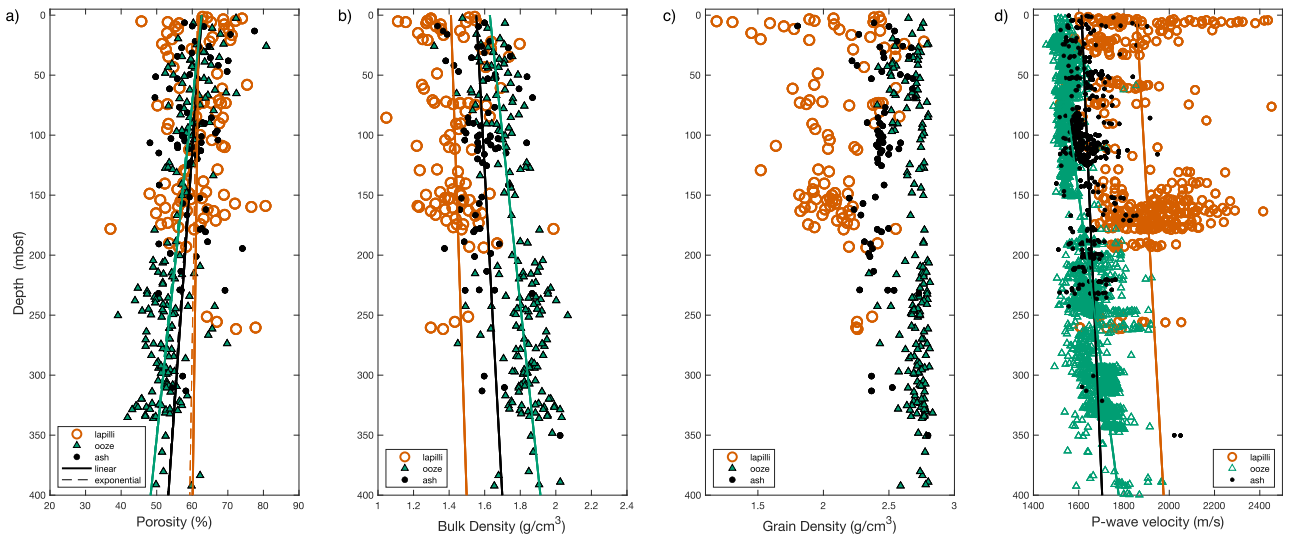

Figure 4. (a) Porosity ϕ, (b) bulk density ρ_b, (c) grain density ρ_g, and (d) P-wave velocity V_p from Sites U1589–U1593 and U1598–U1600 along with linear best-fits for ϕ, ρ_b and V_p (fitted parameters listed in Table 2) and exponential best-fits for ϕ (fitted parameters in the main text). Panels (a–c) show moisture and density data. Panel d shows P-wave gantry data and, because there is much more data, the symbols for ooze are not filled.

exponentially with depth (Athy, 1930), though power law models may fit data better over a broader range of porosity (Baldwin & Butler, 1985) and some studies fit data with quadratic functions (Hamilton, 1976). We fit porosity as a function of depth with an exponential function

$$\phi(z) = \phi_0 e^{-z/\delta}. \quad (1)$$

For the lapilli, ash, and ooze, best-fits for Equation 1 are $\phi_0 = 61.5 \pm 1.0$, 62.5 ± 1.0 and 62.7 ± 1.0 % and $\delta = 11 \pm 24$, 2.45 ± 0.90 and 1.53 ± 0.12 km, respectively.

Because of the limited range of values and depths, we also fit bulk density, porosity, and V_p with linear functions relating properties and depth for ash, lapilli, and the other sediments (oozes). Figure 4a shows that the exponential and linear fits are almost indistinguishable over the range of values sampled in the cores, a consequence of the limited range of values in our shallow measurements. Table 2 summarizes the linear fits to the data and the mean grain density for each lithology. Seafloor values in Table 2 are the best-fit values to the data for seafloor depths of 0 mbsf. The decrease of ϕ for the calcareous oozes of 10% over the first $\sim$ 300 mbsf is similar to the decrease documented elsewhere before the ooze-to-chalk transition (Audet, 1995; Bassinot et al., 1993; Schlanger & Douglas, 1975).

Oozes compact more rapidly with increasing depth compared to volcaniclastic sediments, and their V_p increases more rapidly with increasing depth. $d\rho_b/dz$ and dV_p/dz for the calcareous oozes are more than double those of

Table 2
Physical Properties From Basin Sites U1589–U1593 and U1598–U1600

Material	Seafloor bulk density ρ_b (g/cm^3)	$d\rho_b/dz$ (g/cm^3 per km)	Seafloor porosity ϕ (%)	$d\phi/dz$ (% per km)	Grain density (g/cm^3)	Seafloor V_p (m/s)	dV_p/dz (m/s per km)
ooze	1.629 ± 0.015	0.711 ± 0.059	62.6 ± 0.7	-35.9 ± 2.9	2.700 ± 0.007	1494 ± 3	706 ± 12
	$n = 193$					$n = 1852$	
ash	1.553 ± 0.026	0.365 ± 0.184	62.7 ± 1.3	-23.5 ± 8.9	2.443 ± 0.017	1613 ± 7	228 ± 51
	$n = 71$					$n = 480$	
lapilli	1.410 ± 0.027	0.220 ± 0.217	61.8 ± 1.4	-4.3 ± 11.4	2.087 ± 0.031	1855 ± 17	299 ± 125
	$n = 96$					$n = 377$	

Note. $\pm$ shows the standard error from the regression.

volcaniclastic lapilli. The change in porosity $d\phi/dz$ is almost an order of magnitude larger for the oozes compared to lapilli. Whereas at the shallowest depth V_p for oozes is lower than that for volcaniclastic materials, at depths of a few hundred meters V_p for oozes exceeds that of ash. For the volcaniclastic deposits, the lapilli have lower bulk and grain densities than ash but higher V_p. Porosity changes very little with depth for volcanic lapilli.

4.4. Imaging Isolated Vesicles Inside Pumice Clasts

The low grain densities of volcaniclastic sediments (Figure 4) require fully isolated vesicles inside the volcanic glass. To view the isolated porosity inside pumice clasts, we saturated lapilli from the Archaeos Tuff (Druitt, Kutterolf, Ronge, Hübscher, et al., 2024), recovered from Site U1591 at a depth of 72 mbsf in Hole A. We imaged the spatial distribution of solids, water and gas with X-ray computed microtomography and segmented the gray scale images of X-ray absorption into three phases: solids, liquid water, and gas. Figure 5 shows that some vesicles are water-filled, with others (isolated vesicles) remaining gas-filled. For the particular clast and subregion shown, the volume fraction of solids, water and gas are 37.6%, 52.9%, and 9.5%, respectively. At the burial depths of our samples, pumice clasts have not been crushed, and preserve isolated vesicles as documented by the grain densities (Figure 4) and seen in the microtomography images (Figure 5).

5. Discussion

Physical properties are now routinely measured on marine sediment, including density, magnetic susceptibility, thermal conductivity, shear strength, and seismic velocity. Collectively, physical properties can be used to interpret seismic reflection data and correlate lithologies, model heat transport, assess submarine slope stability, and quantify sedimentation rates, compaction, and some diagenetic processes. Here we studied the porosity, bulk density, and P-wave velocity of volcaniclastic sediment. Our results identify several unusual trends and, hence, questions that we now seek to explain:

1. Why do volcaniclastic lapilli deposits have higher V_p and lower ρ_b than ash-sized volcaniclastic deposits?
2. Why do volcaniclastic sediments have higher velocities than oozes despite similar porosities and elastic moduli of the solid components?
3. Why do volcaniclastic sediments compact more slowly with increasing depth than other sediments?
4. What are the signatures of volcaniclastic sediments in seismic reflection images?

We address these questions with a combination of granular physics models and observations.

In general, even though bulk density appears in the denominator of the equation for V_p (Equation A8), in sediments and rocks without substantial gas-filled void space, elastic moduli increase more with density such that V_p increases as ρ_b increases (Gardner et al., 1974; Hamilton, 1978). For gas-rich sediments in which the gas is outside the particles, the gas lowers the seismic velocity for a given bulk density (Kim et al., 2014), the opposite of what we document for volcanic clasts. If elastic moduli of bulk ash and lapilli samples were the same, the ratio of V_p would be proportional to the square root of the inverse of the bulk density ratio, and thus 8.2% higher for lapilli. In contrast to this expectation, the mean measured V_p of lapilli is 15.2% higher than that of ash, implying that some properties of the lapilli deposits lead to greater sediment elastic moduli.

5.1. Implications of Granular Physics Models

Granular media rock physics models allow sediment properties to be used to model seismic velocities. We use granular physics models because our sediment is unconsolidated, including the calcareous oozes. To assess whether we expect these models to provide reasonable estimates, we first compare measured and modeled V_p for the non-volcanic oozes. Here, we use calcite elastic moduli (Table A1) for the solid particles and compute V_p from the porosity using the Hertz-Mindlin rock physics model and Gassmann fluid substitution (Appendix A). We compare the model with measurements on ooze samples outside the caldera at depths between 10 and 100 m, the same depth range for which we have data for the volcaniclastic samples (number of measurements $n = 481$). To generate a modeled distribution of V_p, we randomly sample from a normal distribution of porosity and grain density using the means and standard deviations in Table 1 and assume depths from 10 to 100 m to compute P.

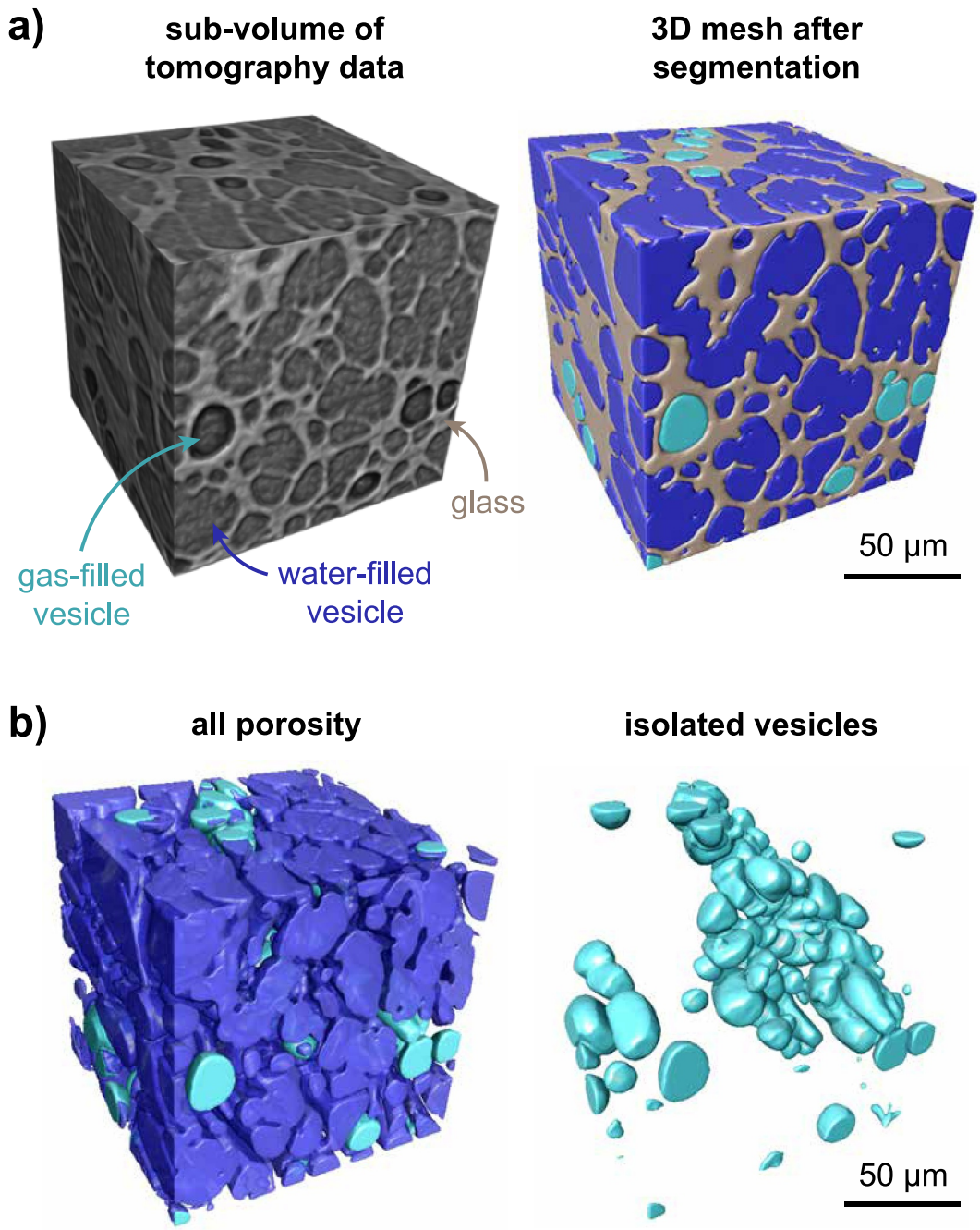

Figure 5. (a) Left: Sub-volume of three-dimensional X-ray computed microtomography images of a pumice clast from the Archaeos Tuff eruption (Figure 3). Gas-filled vesicles are dark gray, water-filled vesicles are medium gray, and the glass is light gray, where the grayscale intensity is proportional to X-ray absorption. Cube is approximately 150 microns on each side. Voxel linear dimension of original tomography data is 0.635 microns. Right: 3D rendering of the solids (glass and any crystals) in gray, water-filled vesicles in dark blue, and gas-filled vesicles in cyan. (b) 3D rendering of all vesicles (left) and isolated vesicles (right), highlighting the isolated vesicles (cyan) that lead to low grain density and low bulk density in volcanic sediments. Scale bars are approximate due to perspective. Images collected on beamline 8.3.2 of the Advanced Light Source using 28 keV monochromatic X-rays.

Figure 6 compares the modeled and measured distribution of V_p. We measured $V_p = 1545.5 \pm 35.6$ m/s and the modeled values are $V_p = 1547.3 \pm 32.3$ m/s. Given the good agreement–without making any adjustments to the models or mineral elastic moduli–we next apply this granular physics modeling approach to the more complex situation where the sediment consists of porous volcanic clasts that contain internal water and gas-filled vesicles.

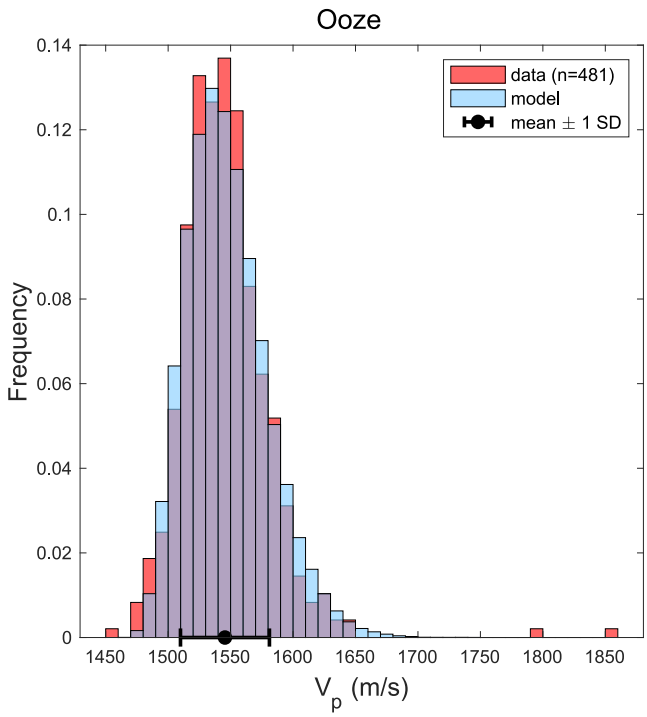

Figure 6. Modeled and measured V_p for lithologies classified as oozes from Sites U1589–U1593 and U1598–U1600 and depths from 10 to 100 mbsf. The purple color shows the overlap of data and model histograms. The symbol with error bars shows the mean measured value and ± one standard deviation.

For the volcanic clasts, some fraction of the measured porosity (water that could be evaporated) consists of water-filled pores inside the clasts. We thus refer to the intergranular porosity of the bulk sediments contained outside of clasts as external porosity, and distinguish between connected and isolated vesicles inside clasts that combined make up the internal porosity (Figure 2). The isolated porosity inside volcanic clasts has been of long-standing interest because it can provide insights into magma vesiculation (Colombier et al., 2023), fragmentation (Rotella et al., 2013), fluidization (Formenti & Druitt, 2003), flow (Akamatsu et al., 2025; Saar & Manga, 1999), and ascent processes (Bonechi et al., 2024; Giachetti et al., 2010). For the solid components (glass and crystals), we used the highest values of measured grain densities, $\rho_s = 2.72$ g/cm^3. The measured grain density ρ_g (mass of glass and crystals divided by the volume of glass, crystals, and isolated vesicles) is lowered from ρ_s owing to isolated gas-filled vesicles within the clasts. The isolated vesicles inside the clasts give rise to grain densities ρ_g that can be substantially lower than ρ_s (Figure 4). Grain densities in pumice from submarine eruptions can be less than 1.03 g/cm^3 (Manga et al., 2018; Mitchell et al., 2021; Takeuchi et al., 2024), but such clasts would float on the sea surface and are not deposited in submarine settings and hence not present in our cores.

Elastic moduli of the clasts are computed using the mean of the Hashin-Shtrikman-Walpole bounds for a solid containing water and gas inclusions (Appendix A). We then use the Hertz-Mindlin model and Gassmann fluid substitution to model V_p. We randomly sample porosity and grain density from the measured distribution and depth from 20 to 100 m and require that the bulk sediment porosity outside the clasts is >10% to avoid unrealistic solutions. Figures 7a and 7c show the modeled and measured V_p distributions. Overall, the mean and distributions are similar, but the measurements are not normally distributed (though the number of samples of porosity and density measurements is modest, around 30 for each type of sediment).

Figures 7b and 7d show the distributions of modeled external porosity and water-filled and gas-filled porosities inside the clasts that lead to V_p within one standard deviation of the measured mean. For the lapilli, the mean external porosity is 31.8% (much lower than ooze porosity shown in Figure 4). The mean internal porosity of clasts is 63.4%. Of that porosity, 25.5% (isolated porosity divided by total clast porosity) consists of isolated gas-filled vesicles. This is not unreasonable for pumice clasts (Colombier et al., 2017). Notably, submarine eruptions produce pumice with relatively low connectivity at high porosity compared with subaerial eruptions (Ward et al., 2025). Pore properties were measured on individual Archaeos Tuff pumice clasts from some of these cores, and these have an isolated pore fraction of 16% (Druitt, Kutterolf, Ronge, Hübscher, et al., 2024), a bit lower than the mean from the calera sites. The isolated pore fraction in the Archaeos Tuff clast shown in Figure 5 is 15.2%, and the grain density is 2.17 g/cm^3–similar the whole clast measurements in Druitt, Kutterolf, Ronge, Hübscher, et al. (2024) and MAD measurements (Figure 4), respectively.

For the ash, the external porosity required to match the measured V_p and density is higher, 51.3%, with a clast porosity of 30.3%. Of the internal porosity, 24.8% consists of isolated gas-filled vesicles, a similar fraction as the lapilli, though the total internal porosity is half the value for lapilli.

The granular physics models are derived for idealized models of monodisperse spherical particles with homogeneous and isotropic properties. Real sediments differ from these assumptions, and volcanic clasts will have porosities and shapes that may vary with size. The results shown in Figure 7 are thus not expected to be accurate but should capture general trends, and these models perform well in explaining seismic velocities of marine sediments (Figure 6) including volcaniclastic sediment (Hornbach et al., 2015; Hornbach & Manga, 2014). In particular, the modeled greater internal porosity of lapilli compared to ash is expected. Further, in the lapilli deposits, having smaller ash-sized particles in the inter-lapilli pore space would reduce the external porosity, as

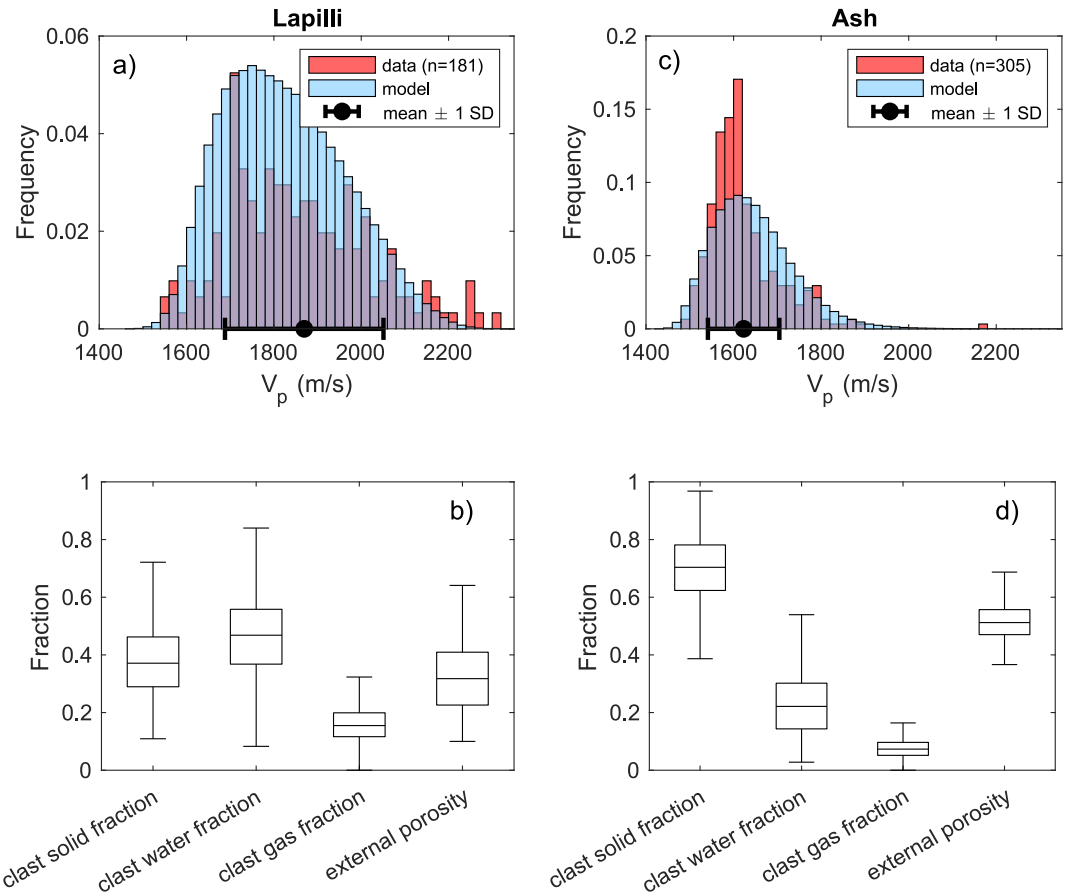

Figure 7. Modeled and measured V_p for lithologies classified as volcaniclastic and (a) lapilli and (c) ash sizes, from Sites U1594–U1597. The symbols with error bars show the mean measured value and ± one standard deviation. Purple color shows overlap of data and model histograms. Box plots for (b) lapilli and (d) ash showing the modeled external porosity (pore fraction outside of clasts), and the fraction of clast volumes that are solid, water, and gas (the solid, water, and gas fractions in the clast sum to one). The line in the middle of each box shows the median, the box spans the 25%–75% quartiles, the bars indicate the range of values, and outliers are not shown.

we find. We note that the binary separation of volcaniclastic sediment into ash and lapilli, based on the shipboard characterization, does not account for the range of sizes and sorting within these two size categories (and might be responsible for some of the scatter about trends).

In summary, the higher V_p in volcaniclastic sediment arises from both isolated vesicles inside clasts that lower bulk density and higher sediment elastic moduli that result from smaller amounts of external porosity surrounding clasts.

5.2. Origins and Implications of Differential Compaction of Volcaniclastic Sediment

Over the age ranges and depths of our sediments, we argue that there are two primary reasons that volcaniclastic sediments compact more slowly with increasing depth than the uncemented oozes. First, the external porosity of volcaniclastic deposits is lower than that of our calcareous oozes, especially for lapilli, so less compaction is possible. Second, the external surface of pumice is rough because of the vesicular texture of the clasts. Rearranging rough particles to enable compaction is more difficult than for smooth particles. A reduced failure susceptibility of volcanic material has also been attributed to volcanic clast roughness, angularity, and low crushability at low effective confining stresses (Wiemer & Kopf, 2017), values of stress that are similar to those of the deposits we studied.

We do not currently have permeability measurements or relevant results from consolidation tests to assess the effects of differential compaction of the calcareous oozes and volcaniclastic sediment in the South Aegean Arc. A small number of ooze samples were extracted, however, for such tests and will be the subject of a future study.

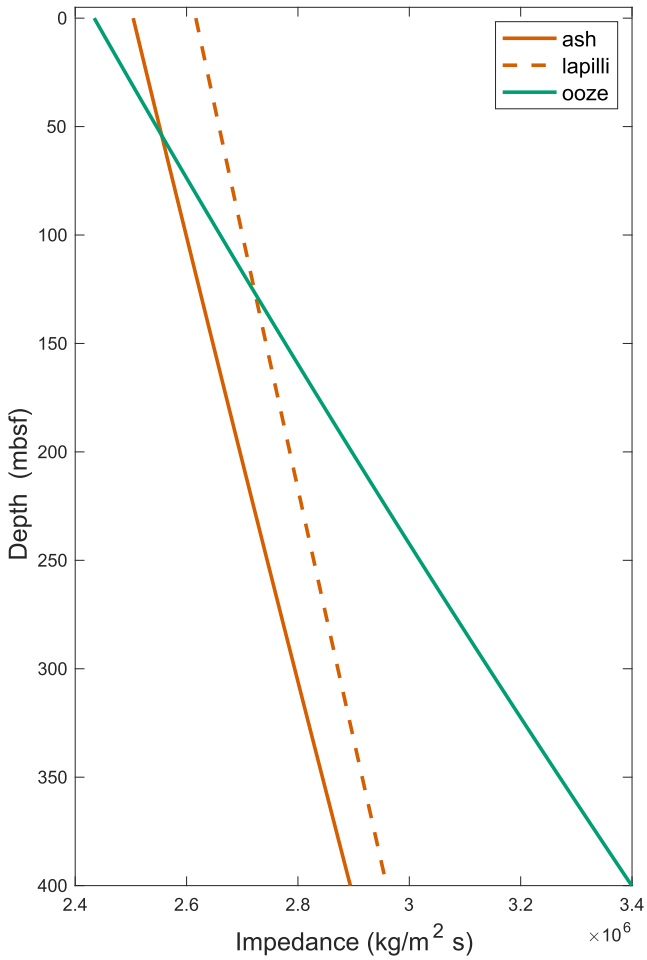

Figure 8. Impedance $(V_p\rho_b)$ for uncemented volcaniclastic sediment and oozes. The impedance of oozes is smaller than volcaniclastic sediment at shallowest depths but higher at depths greater than ~50–150 m, which will lead to depth-dependent differences in how stratigraphic boundaries will be imaged.

Our measurements identify the preservation of isolated gas-filled vesicles in volcaniclastic deposits. The differential compaction rates we observe – with oozes becoming increasingly more dense, and presumably less permeable, while volcaniclastic layers maintain their porosity – may create conditions where pore fluids become trapped provided the permeability of the oozes is low enough (Gatter et al., 2021), helping maintain vesicular textures and potentially generating zones of elevated pore pressure (Cukur et al., 2024). This mechanism might have implications for submarine slope stability and drilling hazard assessment, particularly in volcanic arc settings where alternating ooze and volcaniclastic sequences are common. For example, Harders et al. (2010) suggested that the collapse of pore space in uncompacted and sheared volcaniclastic layers, initiated, for example, by earthquakes, may promote translational sliding and slope failure. Pumiceous sands initially contract under cyclic loading, though they dilate after a few cycles (Asadi et al., 2018). Future studies would ideally include direct pore pressure measurements and permeability testing to evaluate this hypothesis and its implications for geohazard assessment.

5.3. Seismic Signatures of Volcaniclastic Sediments in Rift Basins

The differential compaction of volcaniclastic and other sediment, and their effects on V_p and ρ_b, affect how seismic impedance varies with depth and, hence, how seismic imaging will see impedance contrasts between different deposits and formations. Impedance can be calculated from the trends summarized in Table 2. In particular, oozes have the lowest impedance in the upper ~50 m but higher values at greater depths for volcanic ash, or depths greater than ~150 m for lapilli (Figure 8).

The distinct contrasts between volcaniclastic and non-volcanic deposits are most clearly visible in seismic images from the Anhydros Basin east and Anafi Basin southeast of Santorini (Figure 1), which represent major rift basins (Figure 9). Both basins are characterized by a major unconformity, designated as horizon csk1, which separates the lower, pelagic-dominated Unit CSK2 from the overlying volcaniclastic-dominated Unit CSK1 (Preine, Hübscher, et al., 2022). This boundary marks a significant rift pulse around 300–250 ka that created the accommodation space for subsequent volcanic infilling (Metcalfe, Druitt, Pank, Kutterolf, Preine, Kelfoun, et al., 2025; Metcalfe, Druitt, Pank, Kutterolf, Preine, Beethe, et al., 2025). Unit CSK2 consists primarily of calcareous oozes with minor intercalated tephra layers and is characterized by well-stratified, medium-amplitude reflections in seismic profiles (Preine, Hübscher, et al., 2022). In marked contrast, Unit CSK1 comprises a succession of thick volcaniclastic megabeds derived from explosive eruptions of Santorini and Kos (Metcalfe, Druitt, Pank, Kutterolf, Preine, Kelfoun, et al., 2025; Metcalfe, Druitt, Pank, Kutterolf, Preine, Beethe, et al., 2025), including the Minoan (~3.6 ka), Cape Riva (~22 ka), Kos Plateau Tuff (KPT) (~161 ka), and Lower Pumice 1 and 2 (~186 and ~177 ka, respectively) with ages from Wulf et al. (2020).

In the Anhydros Basin, volcaniclastic megabeds appear in seismic reflection data as laterally extensive packages with incoherent internal reflections of generally low amplitude, separated by prominent high-amplitude boundary reflections (Figure 9c). A notable exception is the Middle Tuff Sequence, which exhibits more continuous, medium-amplitude reflections and greater internal stratification, similar to those observed in Unit CSK2 (Figure 9c). The Anafi Basin, in contrast, is dominated by an exceptionally thick (~200 m) deposit from the Kos Plateau Tuff (KPT) eruption, accompanied by major deposits of the Minoan, Cape Riva, and Lower Pumice eruptions (Figure 9f). The KPT megabed in the Anafi Basin is characterized by generally low-amplitude reflections with some internal stratification, as well as some more pronounced internal reflection contrasts, including a prominent reflection that marks the transition from coarse-grained ash in the lower portion to finer ash in the upper part (Metcalfe, Druitt, Pank, Kutterolf, Preine, Kelfoun, et al., 2025), and a sharp basal boundary with high reflection amplitudes (Figure 9f).

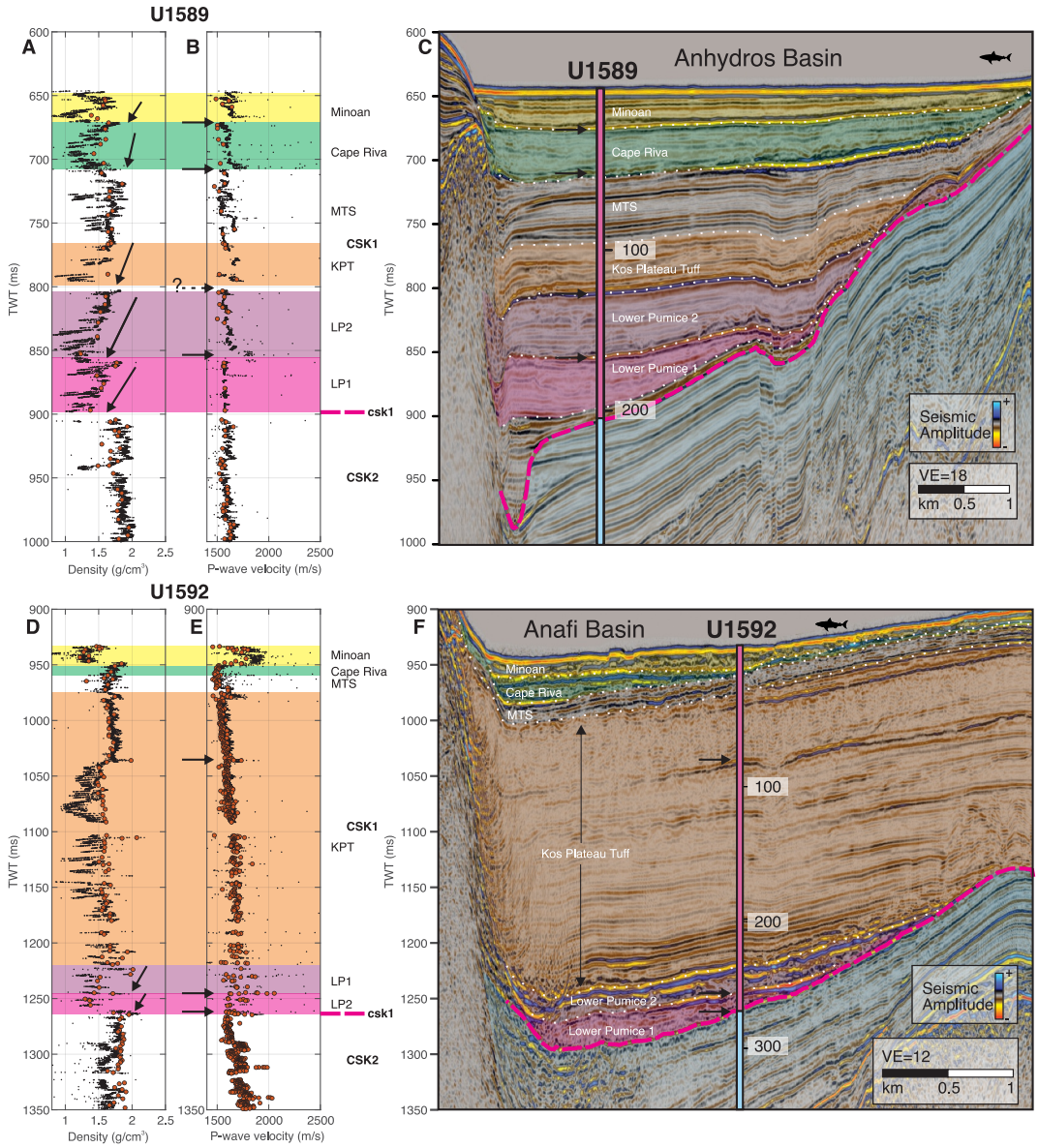

Figure 9. Comparison of physical properties measured at Sites U1589 and U1592 with seismic reflection profiles across the Anhydros and Anafi Basins. (a, b, d, e) Density and P-wave velocity measurements shown on a composite depth scale converted to two-way travel time for direct comparison with seismic reflection data. Orange circles show the discrete measurements we analyze in current study, while black circles correspond to measurements made on unsplit cores at 2.5 cm intervals measured with the Whole Round Multi Sensing Logger (Kutterolf et al., 2024). Arrows in panels (a, d) highlight density trends within individual volcanic megabeds; arrows in (b, e) mark distinct peaks in P-wave velocity. Semi-transparent color bands delineate volcaniclastic units, including LP1 (Lower Pumice 1), LP2 (Lower Pumice 2), KPT (Kos Plateau Tuff), and MTS (Middle Tuff Sequence), based on Metcalfe, Druitt, Pank, Kutterolf, Preine, Beethe, et al. (2025). The dashed blue horizontal line denotes the major unconformity csk1, separating seismostratigraphic Units CSK1 and CSK2. Panels (c, f) Seismic reflection profiles through the Anhydros and Anafi Basins, with core-seismic integration after (Preine et al., 2025). Ticks at the drill sites indicate recovered depths (in meters below seafloor). High-amplitude reflections are indicated by arrows; semi-transparent colors highlight the same volcanic megabeds shown in the physical property plots. VE: vertical exaggeration. For profile locations, see Figure 1.

These seismic units correlate well with physical property data from core and downhole measurements (Figure 9). Each volcaniclastic megabed exhibits a characteristic fining-upward trend, with density increasing toward the top (see arrows in Figures 9a and 9d). Spikes in P-wave velocity are consistently observed at the base of each megabed (see arrows in Figures 9b and 9e), corresponding to coarse-grained pumice lapilli layers that produce

high acoustic impedance contrasts compared to the underlying sediments, which manifest as strong basal reflections in the seismic profiles. Only the base of the KPT deposit in the Anafi Basin reveals no P-wave velocity spike as the base was not recovered at U1589 (see dashed arrow with question mark in Figure 9b), but is clearly associated with a high-amplitude reflection visible in the seismic image (Figure 9c). In some cases, such as the Cape Riva base in the Anafi Basin, lateral variations in reflection amplitude suggest changes in the concentration or grain size of basal lapilli across the basin. The most basal reflections of the megabeds are conformable on underlying strata, indicating non-erosional emplacement within pre-existing accommodation space.

Collectively, these observations highlight how the physical characteristics of volcaniclastic sediments, especially coarse basal layers and gradational trends, are systematically imprinted in their seismic appearance and strongly contrast with pelagic sedimentation, offering a unique diagnostic framework for identifying and differentiating explosive eruptive products in subsurface seismic records.

6. Conclusions

Based on a comparison of shipboard density measurements and available logging data, discrete measurements of density in recovered cores appear to document in situ values. At seafloor depths, the bulk densities of volcaniclastic sediments are lower than, and the P-wave velocity is greater than, that of other cored marine sediments. Volcaniclastic materials, however, compact more slowly with increasing depth such that the seismic impedance becomes lower than that of other sediments at depths greater than $\sim 50 - 150$ m. Coarse lapilli-sized volcaniclastic deposits have lower bulk density and higher P-wave velocity than finer ash-sized deposits. This difference arises from a lower external porosity of the coarser deposits that increases sediment elastic moduli, combined with a greater proportion of isolated vesicles inside the clasts, which lowers bulk density.

These conclusions come with the caveats that there may be unknown and unquantifiable systematic biases arising from disturbance during coring and core recovery, the inability to successfully make measurements on some recovered materials, and the ability to recover the core itself.

Appendix A: Rock Physics Modeling

To compute the sediment P-wave velocity from measured sediment properties and interpret trends and patterns, we need to know the mineralogy and elastic moduli of the particles (bulk modulus K and shear modulus G) that make up the sediment (Table A1) and then use granular physics models to compute bulk sediment properties. For the volcaniclastic particles, we use the Hashin-Shtrikman-Walpole bounds (Hashin & Shtrikman, 1963; Walpole, 1966) for composite particles to account for pores within the clasts containing water and gas. We then use the Hertz-Mindlin model (Mindlin, 1949) to compute bulk sediment elastic moduli.

The shipboard measurements provide the volume fraction of the sediment that consists of water ϕ, the bulk density of the sediment ρ_b, and the grain density ρ_g. In non-volcanic sediments, the measured porosity usually consists of the pore space surrounding grains. Volcaniclastic particles such as pumice, however, are porous, and some of that internal porosity is filled with water, while some internal porosity consists of isolated gas-filled vesicles. We will use the subscript *clast* to indicate the properties of these clasts that are made of a combination of solids, water, and gas. The subscript S is used to denote values for the solids (minerals and volcanic glass). Thus, the porosity outside clasts is $\phi - f_w$, where f_w is the water fraction of the bulk sediment contained within clasts. The volume fraction of solid materials (minerals, volcanic glass) with density ρ_m is

Table A1
Properties of the Solid Components of the Sediments

Solid phase	Density ρ_s (g/cm^3)	K_s (GPa)	G_s (GPa)	Reference
Ooze (calcite)	2.70	70	20	Mavko and Mukerji (1998)
Volcanic clasts (dacite)	2.72	78.9	32.4	Alidibirov et al. (1997)
Water	1.03	2.34	0	
Gas	0.00129	0.2	0	

$$f_s = \frac{\rho_b}{\rho_m} - \phi \frac{\rho_w}{\rho_m}, \tag{A1}$$

where ρ_w is the water density. The volume fraction of the sediment that is gas is

$$f_{gas} = 1 - \phi - f_s. \tag{A2}$$

All gas is assumed to be contained in isolated vesicles inside clasts.

A1. Elastic Moduli of Clasts

The elastic properties of volcanic clasts are affected by the water and gas-filled vesicles inside the clasts. The precise value depends on the geometry of the pores, in addition to the elastic moduli and density of the pore-filling phases and the solids. The Hashin-Shtrikman-Walpole bounds provide upper and lower values and are computed using the code provided in Abers and Hacker (2016). In the modeling, we use the average of the upper and lower bounds for moduli of the clasts and use the subscript *clast* to indicate the Hashin-Shtrikman-Walpole values for particles.

A2. Elastic Moduli of Sediments

The Hertz-Mindlin model (Mindlin, 1949) for granular materials computes elastic moduli by computing the stiffness of packings of randomly organized identical spheres

$$K_{HM} = \left[\frac{C^2 (1 - \phi + f_w)^2 G_{clast}^2}{18\pi^2 (1 - \nu_{clast})^2} P \right]^{1/3} \tag{A3}$$

and

$$G_{HM} = \frac{(5 - 4\nu_{clast})}{5(2 - \nu_{clast})} \left[\frac{3C^2 (1 - \phi + f_w)^2 G_{clast}^2}{2\pi^2 (1 - \nu_{clast})^2} P \right]^{1/3}, \tag{A4}$$

where C is the coordination number of the grains, P is the effective pressure (lithostatic-hydrostatic), and ν_{clast} is the Poisson ratio of the clasts. C is computed from (Murphy, 1982)

$$C = 20 - 34(\phi - f_w) + 14(\phi - f_w)^2. \tag{A5}$$

A3. Gassmann Fluid Substitution

The Hertz-Mindlin model computes the dry-frame moduli K_{HM} and G_{HM}. For water-saturated sediments, the Gassmann-Biot (Gassmann, 1951) theory accounts for fluid substitution,

$$\frac{K_{sat}}{K_{clast} - K_{sat}} = \frac{K_{HM}}{K_{clast} - K_{HM}} + \frac{K_w}{(\phi - f_w)(K_{clast} - K_w)} \tag{A6}$$

and

$$G_{sat} = G_{HM}. \tag{A7}$$

The Gassmann-Biot equation applies to low enough frequencies such that the pore pressure produced by seismic waves equilibrates throughout the pore space. This approximation may not be reached for the ultrasonic waves used for shipboard measurements, and the model can perform less well (Mavko & Mukerji, 1998).

A4. Computing Seismic Velocity

The bulk sediment elastic moduli (K_{sat} and G_{sat}) and bulk density (ρ_b) are used to compute the P-wave velocity V_p,

$$V_p = \sqrt{\frac{K_{sat} + \frac{4}{3}G_{sat}}{\rho_b}}. \tag{A8}$$

Conflict of Interest

The authors declare no conflicts of interest relevant to this study.

Data Availability Statement

Data plotted in the figures and used in analyses are tabulated in Druitt, Kutterolf, Ronge, et al. (2024). Plots were created using Matlab. Linear fits in Table 2, and exponential fits reported in the main text, were calculated in Microsoft Excel. The Matlab codes for granular physics calculations used in Figures 6 and 7 are available from Wright and Manga (2025). Figure 1 was created based on publicly available digital elevation models (DEMs), complemented by data sets from EMODnet and PROTEUS. The data can be accessed via EMODnet Bathymetry Consortium (2018). In addition, high-resolution seismic reflection data shown in Figure 9 were acquired during the POS538 research cruise and can be obtained from Karstens and Preine (2023). Artificial Intelligence was not knowingly used for any of this research except for the machine learning segmentation of the X-ray computed tomography images into gas, liquid water, and solid phases (see Methods).

Acknowledgments
We thank the crew, staff, and technicians on JOIDES Resolution Expedition 398. We acknowledge support from the National Science Foundation (OCE1326927), travel support for US scientists by the U.S. Science Support Program, as well as European scientists by IODP-Germany and ECORD (GG009393-04), and the Université Clermont Auvergne in France. M. Manga, V. Wright, and T. Cadena received additional support from the Miller Institute and Canadian Institute for Advanced Research (CIFAR) Earth4D. S. Kutterolf is supported by the German Research Foundation (DFG527924707). X-ray tomography was made possible with the support of the Department of Energy Advanced Light Source beamline 8.3.2. We thank the editor and two reviewers for suggestions and comments.

References

Abers, G. A., & Hacker, B. R. (2016). A matlab toolbox and excel workbook for calculating the densities, seismic wave speeds, and major element composition of minerals and rocks at pressure and temperature. *Geochemistry, Geophysics, Geosystems*, *17*(2), 616–624. https://doi.org/10.1002/2015GC006171

Akamatsu, Y., Suzuki, T., Tada, N., Sawayama, K., Ichihara, H., Katayama, I., et al. (2025). Variations in pore structure in subaerial lava flows at nishinoshima, Japan, inferred from physical properties. *Journal of Volcanology and Geothermal Research*, *458*, 108262. https://doi.org/10.1016/j.jvolgeores.2024.108262

Alidibirov, M., Dingwell, D., Stevenson, R., Hess, K.-U., Webb, S., & Zinke, J. (1997). Physical properties of the 1980 Mount St. Helens cryptodome magma. *Bulletin of Volcanology*, *59*(2), 103–111. https://doi.org/10.1007/s004450050178

Arculus, R., Ishizuka, O., Bogus, K., Aljahdali, M., Bandini-Maeder, A., Barth, A., & others (2015). Expedition 351 summary. *Proceedings of the International Ocean Discovery Program*, *351*. https://doi.org/10.14379/iodp.proc.351.102.2015

Asadi, M. S., Asadi, M. B., Orense, R. P., & Pender, M. J. (2018). Undrained cyclic behavior of reconstituted natural pumiceous sands. *Journal of Geotechnical and Geoenvironmental Engineering*, *144*(8), 04018045. https://doi.org/10.1061/(ASCE)GT.1943-5606.0001912

Athy, L. F. (1930). Density, porosity, and compaction of sedimentary rocks. *AAPG Bulletin*, *14*(1), 1–24. https://doi.org/10.1306/3D93289E-16B1-11D7-8645000102C1865D

Audet, D. M. (1995). Modelling of porosity evolution and mechanical compaction of calcareous sediments. *Sedimentology*, *42*(2), 355–373. https://doi.org/10.1111/j.1365-3091.1995.tb02106.x

Baldwin, B., & Butler, C. O. (1985). Compaction curves. *AAPG Bulletin*, *69*(4), 622–626. https://doi.org/10.1306/AD462547-16F7-11D7-8645000102C1865D

Bassinot, F., Marsters, J. C., Mayer, L. A., & Wilkens, R. H. (1993). Variations of porosity in calcareous sediments from the Ontong Java Plateau (Vol. *130*, pp. 653–661).

Blum, P. (1997). Physical properties handbook: A guide to the shipboard measurement of physical properties of deep-sea cores. ODP technical notes 26. *Ocean Drilling Program*

Bonechi, B., Polacci, M., Arzilli, F., La Spina, G., Hazemann, J.-L., Brooker, R. A., et al. (2024). Direct observation of degassing during decompression of basaltic magma. *Science Advances*, *10*(33), eado2585. https://doi.org/10.1126/sciadv.ado2585

Bredehoeft, J., & Hanshaw, B. (1968). On the maintenance of anomalous fluid pressures: I. thick sedimentary sequences. *Geological Society of America Bulletin*, *79*(9), 1097–1106. https://doi.org/10.1130/0016-7606(1968)79[1097:OTMOAF]2.0.CO;2

Busby, C. J., Tamura, Y., Blum, P., Guèrin, G., Andrews, G. D., Barker, A. K., et al. (2017). The missing half of the subduction factory: Shipboard results from the Izu Rear Arc, IODP Expedition 350. *International Geology Review*, *59*(13), 1677–1708. https://doi.org/10.1080/00206814.2017.1292469

Cantner, K., Carey, S., & Nomikou, P. (2014). Integrated volcanologic and petrologic analysis of the 1650 ad eruption of Kolumbo submarine volcano, Greece. *Journal of Volcanology and Geothermal Research*, *269*, 28–43. https://doi.org/10.1016/j.jvolgeores.2013.10.004

Carey, R. J., Butterfield, D. A., & Clark, M. R. (2025). Submarine volcanic eruptions and their impacts on hydrothermal systems and biological communities. *Annual Review of Earth and Planetary Sciences*, *53*(1), 397–423. https://doi.org/10.1146/annurev-earth-040522-095654

Cas, R. A., & Wright, J. V. (1991). Subaqueous pyroclastic flows and ignimbrites: An assessment. *Bulletin of Volcanology*, *53*(5), 357–380. https://doi.org/10.1007/BF00280227

Cashman, K. V., & Fiske, R. S. (1991). Fallout of pyroclastic debris from submarine volcanic eruptions. *Science*, *253*(5017), 275–280. https://doi.org/10.1126/science.253.5017.275

Cassidy, M., Watt, S. F., Palmer, M. R., Trofimovs, J., Symons, W., Maclachlan, S. E., & Stinton, A. J. (2014). Construction of volcanic records from marine sediment cores: A review and case study (Montserrat, West Indies). *Earth-Science Reviews*, *138*, 137–155. https://doi.org/10.1016/j.earscirev.2014.08.008

Clare, M. A., Yeo, I. A., Watson, S., Wysoczanski, R., Seabrook, S., Mackay, K., et al. (2023). Fast and destructive density currents created by ocean-entering volcanic eruptions. *Science*, *381*(6662), 1085–1092. https://doi.org/10.1126/science.adi3038

Colombier, M., Manga, M., Wright, H., Bernard, B., deGraffenried, R., Caceres, F., et al. (2023). Pre-eruptive outgassing and pressurization, and post-fragmentation bubble nucleation, recorded by vesicles in breadcrust bombs from vulcanian activity at Guagua Pichincha volcano, Ecuador. *Journal of Geophysical Research: Solid Earth*, *128*(9), e2023JB026775. https://doi.org/10.1029/2023JB026775

Colombier, M., Wadsworth, F. B., Gurioli, L., Scheu, B., Kueppers, U., Di Muro, A., & Dingwell, D. B. (2017). The evolution of pore connectivity in volcanic rocks. *Earth and Planetary Science Letters*, *462*, 99–109. https://doi.org/10.1016/j.epsl.2017.01.011

Comet Technologies Canada Inc. (2024). Dragonfly 3D world version 2024.1.0.1597. Retrieved from https://www.theobjects.com/dragonfly

Cukur, D., Um, I.-K., Buchs, D. M., Kim, S.-P., Kong, G.-S., Chun, J.-H., et al. (2024). Submarine landslides on the eastern South Korea plateau—Do pumice-rich tephra layers control slope stability? *Marine Geology*, *467*, 107205. https://doi.org/10.1016/j.margeo.2023.107205

Dickinson, G. (1953). Geological aspects of abnormal reservoir pressures in Gulf Coast Louisiana. *AAPG Bulletin*, *37*(2), 410–432. https://doi.org/10.1306/5CEADC6B-16BB-11D7-8645000102C1865D

Druitt, T. H., Edwards, L., Mellors, R., Pyle, D., Sparks, R., Lanphere, M., et al. (1999). Santorini volcano. *Geological Society, London, Memoirs*, *19*(1). https://doi.org/10.1144/GSL.MEM.1999.019.01.12

Druitt, T. H., Kutterolf, S., Ronge, T., et al. (2024). Hellenic Arc volcanic field. *Proceedings of the International Ocean Discovery Program Expedition reports*, *398*. https://doi.org/10.14379/iodp.proc.398.2024

Druitt, T. H., Kutterolf, S., Ronge, T. A., Beethe, S., Bernard, A., Berthod, C., et al. (2024a). Expedition 398 summary. *Proceedings of the International Ocean Discovery Program*, *398*. https://doi.org/10.14379/iodp.proc.398.101.2024

Druitt, T. H., Kutterolf, S., Ronge, T. A., Beethe, S., Bernard, A., Berthod, C., et al. (2024b). Site U1589. *Proceedings of the International Ocean Discovery Program*, *398*. https://doi.org/10.14379/iodp.proc.398.103.2024

Druitt, T. H., Kutterolf, S., Ronge, T. A., Hübscher, C., Nomikou, P., Preine, J., et al. (2024). Giant offshore pumice deposit records a shallow submarine explosive eruption of ancestral Santorini. *Communications Earth & Environment*, *5*(1), 24. https://doi.org/10.1038/s43247-023-01171-z

Dutkiewicz, A., Müller, R. D., O'Callaghan, S., & Jónasson, H. (2015). Census of seafloor sediments in the world's ocean. *Geology*, *43*(9), 795–798. https://doi.org/10.1130/G36883.1

EMODnet Bathymetry Consortium. (2018). EMODnet digital bathymetry (DTM) 2018. Retrieved from https://sextant.ifremer.fr/record/18ff0d48-b203-4a65-94a9-5fd8b0ec35f6/doi:10.12770/18ff0d48-b203-4a65-94a9-5fd8b0ec35f6

Fauria, K. E., Manga, M., & Wei, Z. (2017). Trapped bubbles keep pumice afloat and gas diffusion makes pumice sink. *Earth and Planetary Science Letters*, *460*, 50–59. https://doi.org/10.1016/j.epsl.2016.11.055

Fisher, R. V. (1961). Proposed classification of volcaniclastic sediments and rocks. *Geological Society of America Bulletin*, *72*(9), 1409–1414. https://doi.org/10.1130/0016-7606(1961)72[1409:PCOVSA]2.0.CO;2

Formenti, Y., & Druitt, T. (2003). Vesicle connectivity in pyroclasts and implications for the fluidisation of fountain-collapse pyroclastic flows, Montserrat (West Indies). *Earth and Planetary Science Letters*, *214*(3–4), 561–574. https://doi.org/10.1016/S0012-821X(03)00386-8

Fowler, A. C., & Yang, X. (1999). Pressure solution and viscous compaction in sedimentary basins. *Journal of Geophysical Research*, *104*(B6), 12989–12997. https://doi.org/10.1029/1998JB900029

Freundt, A., Schindlbeck-Belo, J. C., Kutterolf, S., & Hopkins, J. L. (2023). *Tephra layers in the marine environment: A review of properties and emplacement processes*. Geological Society of London, Special Publications. https://doi.org/10.1144/SP520-2021-50.520

Fuller, S., Carey, S., & Nomikou, P. (2018). Distribution of fine-grained tephra from the 1650 CE submarine eruption of Kolumbo volcano, Greece. *Journal of Volcanology and Geothermal Research*, *352*, 10–25. https://doi.org/10.1016/j.jvolgeores.2018.01.004

Gardner, G., Gardner, L., & Gregory, A. (1974). Formation velocity and density—the diagnostic basics for stratigraphic traps. *Geophysics*, *39*(6), 770–780. https://doi.org/10.1190/1.1440465

Gassmann, F. (1951). Elastic waves through a packing of spheres. *Geophysics*, *16*(4), 673–685. https://doi.org/10.1190/1.1437718

Gatter, R., Clare, M., Kuhlmann, J., & Huhn, K. (2021). Characterisation of weak layers, physical controls on their global distribution and their role in submarine landslide formation. *Earth-Science Reviews*, *223*, 103845. https://doi.org/10.1016/j.earscirev.2021.103845

Giachetti, T., Druitt, T. H., Burgisser, A., Arbaret, L., & Galven, C. (2010). Bubble nucleation, growth and coalescence during the 1997 vulcanian explosions of Soufrière Hills volcano, Montserrat. *Journal of Volcanology and Geothermal Research*, *193*(3–4), 215–231. https://doi.org/10.1016/j.jvolgeores.2010.04.001

Hamilton, E. L. (1976). Variations of density and porosity with depth in deep-sea sediments. *Journal of Sedimentary Research*, *46*(2), 280–300. https://doi.org/10.1306/212F6F3C-2B24-11D7-8648000102C1865D

Hamilton, E. L. (1978). Sound velocity–density relations in sea-floor sediments and rocks. *Journal of the Acoustical Society of America*, *63*(2), 366–377. https://doi.org/10.1121/1.381747

Hanyu, T., Seama, N., Kaneko, K., Chang, Q., Nakaoka, R., Kiyosugi, K., et al. (2024). Submarine cores record magma evolution toward a catastrophic eruption at Kikai caldera. *Communications Earth & Environment*, *5*(1), 428. https://doi.org/10.1038/s43247-024-01591-5

Harders, R., Kutterolf, S., Hensen, C., Moerz, T., & Brueckmann, W. (2010). Tephra layers: A controlling factor on submarine translational sliding? *Geochemistry, Geophysics, Geosystems*, *11*(5). https://doi.org/10.1029/2009GC002844

Hashin, Z., & Shtrikman, S. (1963). A variational approach to the theory of the elastic behaviour of multiphase materials. *Journal of the Mechanics and Physics of Solids*, *11*(2), 127–140. https://doi.org/10.1016/0022-5096(63)90060-7

Heath, B., Hooft, E., Toomey, D., Papazachos, C., Nomikou, P., Paulatto, M., et al. (2019). Tectonism and its relation to magmatism around santorini volcano from upper crustal P wave velocity. *Journal of Geophysical Research: Solid Earth*, *124*(10), 10610–10629. https://doi.org/10.1029/2019JB017699

Hornbach, M. J., & Manga, M. (2014). The ability of rock physics models to infer marine in situ pore pressure. *Geochemistry, Geophysics, Geosystems*, *15*(12), 4769–4780. https://doi.org/10.1002/2014GC005442

Hornbach, M. J., Manga, M., Genecov, M., Valdez, R., Miller, P., Saffer, D., et al. (2015). Permeability and pressure measurements in Lesser Antilles submarine slides: Evidence for pressure-driven slow-slip failure. *Journal of Geophysical Research: Solid Earth*, *120*(12), 7986–8011. https://doi.org/10.1002/2015jb012061

Hübscher, C., Ruhnau, M., & Nomikou, P. (2015). Volcano-tectonic evolution of the polygenetic Kolumbo submarine volcano/Santorini (Aegean Sea). *Journal of Volcanology and Geothermal Research*, *291*, 101–111. https://doi.org/10.1002/2015JB012061

Johnston, E., Sparks, R., Nomikou, P., Livanos, I., Carey, S., Phillips, J., & Sigurdsson, H. (2015). Stratigraphic relations of santorini's intra-caldera fill and implications for the rate of post-caldera volcanism. *Journal of the Geological Society*, *172*(3), 323–335. https://doi.org/10.1144/jgs2013-114

Jutzeler, M., Clark, A. S., Manga, M., McIntosh, I., Druitt, T., Kutterolf, S., & Ronge, T. A. (2025). Data report: Coring disturbances in advanced piston cores from IODP Expedition 398, Hellenic arc volcanic field. *Proceedings of the International Ocean Discovery Program*, *398*. https://doi.org/10.14379/iodp.proc.398.203.2025

Jutzeler, M., Manga, M., White, J., Talling, P., Proussevitch, A., Watt, S., et al. (2017). Submarine deposits from pumiceous pyroclastic density currents traveling over water: An outstanding example from offshore Montserrat (IODP 340). *Geological Society of American Bulletin*, *129*(3–4), 392–414. https://doi.org/10.1130/B31448.1

Karstens, J., & Preine, J. (2023). 2D seismic reflection data from POSEIDON cruise POS538, offshore Santorini. (Version 1.0) [Dataset]. *PANGAEA*. https://doi.org/10.1594/PANGAEA.956579

Karstens, J., Preine, J., Crutchley, G. J., Kutterolf, S., van der Bilt, W. G., Hooft, E. E., et al. (2023). Revised minoan eruption volume as benchmark for large volcanic eruptions. *Nature Communications*, *14*(1), 2497. https://doi.org/10.1038/s41467-023-38176-3

Kim, G. Y., Narantsetseg, B., Kim, J. W., & Chun, J. H. (2014). Physical properties and micro-and macro-structures of gassy sediments in the inner shelf of SE Korea. *Quaternary International*, *344*, 170–180. https://doi.org/10.1016/j.quaint.2014.01.049

Kutterolf, S., Druitt, T. H., Ronge, T. A., Beethe, S., Bernard, A., Berthod, C., et al. (2024). Expedition 398 methods. *Proceedings of the International Ocean Discovery Program*, *398*. https://doi.org/10.14379/iodp.proc.398.102.2024

Kutterolf, S., Schindlbeck, J., Robertson, A., Avery, A., Baxter, A., Petronotis, K., & Wang, K.-L. (2018). Tephrostratigraphy and provenance from IODP Expedition 352, Izu-Bonin Arc: Tracing tephra sources and volumes from the oligocene to recent. *Geochemistry, Geophysics, Geosystems*, *19*(1), 150–174. https://doi.org/10.1002/2017gc007100

Le Friant, A., Ishizuka, O., Boudon, G., Palmer, M., Talling, P., Villemant, B., et al. (2015). Submarine record of volcanic island construction and collapse in the Lesser Antilles Arc: First scientific drilling of submarine volcanic island landslides by IODP Expedition 340. *Geochemistry, Geophysics, Geosystems*, *16*(2), 420–442. https://doi.org/10.1002/2014GC005652

Manga, M., Fauria, K. E., Lin, C., Mitchell, S. J., Jones, M. P., Conway, C. E., et al. (2018). The pumice raft-forming 2012 havre submarine eruption was effusive. *Earth and Planetary Science Letters*, *489*, 49–58. https://doi.org/10.1016/j.epsl.2018.02.025

Manga, M., Tominaga, M., Preine, J., Ronge, T. A., Beethe, S., Hübscher, C., et al. (2025). Low heat flow in the Anhydros Basin, Aegean Sea, recorded by deep subsurface temperatures. *Geophysical Research Letters*, *52*(13), e2025GL115919. https://doi.org/10.1029/2025GL115919

Manville, V., Németh, K., & Kano, K. (2009). Source to sink: A review of three decades of progress in the understanding of volcaniclastic processes, deposits, and hazards. *Sedimentary Geology*, *220*(3–4), 136–161. https://doi.org/10.1016/j.sedgeo.2009.04.022

Mavko, G., & Mukerji, T. (1998). A rock physics strategy for quantifying uncertainty in common hydrocarbon indicators. *Geophysics*, *63*(6), 1997–2008. https://doi.org/10.1190/1.1444493

Metcalfe, A., Druitt, T., Pank, K., Kutterolf, S., Preine, J., Beethe, S., et al. (2025). Tectonic Modulation of Caldera Volcanism on the South Aegean Volcanic Arc. *Earth and Planetary Science Letters*, 119633. https://doi.org/10.1016/j.epsl.2025.119633

Metcalfe, A., Druitt, T., Pank, K., Kutterolf, S., Preine, J., Kelfoun, et al. (2025). Submarine ash megabed fed by far-traveled, shoreline-crossing pyroclastic currents from a large explosive volcanic eruption. *Science Advances*, *11*(33), eads9642. https://doi.org/10.1126/sciadv.ads9642

Mindlin, R. D. (1949). Compliance of elastic bodies in contact. *Journal of Applied Mechanics*, *16*(3), 259–268. https://doi.org/10.1115/1.4009973

Mitchell, S. J., Fauria, K. E., Houghton, B. F., & Carey, R. J. (2021). Sink or float: Microtextural controls on the fate of pumice deposition during the 2012 submarine Havre eruption. *Bulletin of Volcanology*, *83*, 1–20. https://doi.org/10.1115/1.4009973

Murphy, W. (1982). *Effects of microstructure and pore fluids on the acoustic properties of granular sedimentary materials*. Stanford University.

Nomikou, P., Hübscher, C., Papanikolaou, D., Farangitakis, G. P., Ruhnau, M., & Lampridou, D. (2018). Expanding extension, subsidence and lateral segmentation within the Santorini-Amorgos basins during quaternary: Implications for the 1956 Amorgos events, Central-South Aegean Sea, Greece. *Tectonophysics*, *722*, 138–153. https://doi.org/10.1016/j.tecto.2017.10.016

Nomikou, P., Hübscher, C., Ruhnau, M., & Bejelou, K. (2016). Tectono-stratigraphic evolution through successive extensional events of the Anydros Basin, hosting Kolumbo volcanic field at the Aegean Sea, Greece. *Tectonophysics*, *671*, 202–217. https://doi.org/10.1016/j.tecto.2016.01.021

Nomikou, P., Papanikolaou, D., Alexandri, M., Sakellariou, D., & Rousakis, G. (2013). Submarine volcanoes along the Aegean Volcanic Arc. *Tectonophysics*, *597*, 123–146. https://doi.org/10.1016/j.tecto.2012.10.001

Piper, D., Pe-Piper, G., Perissoratis, C., & Anastasakis, G. (2007). Distribution and chronology of submarine volcanic rocks around Santorini and their relationship to faulting. *Geological Society, London, Special Publications*, *291*(1), 99–111. https://doi.org/10.1144/SP291.5

Portner, R. A., Clague, D. A., Helo, C., Dreyer, B. M., & Paduan, J. B. (2015). Contrasting styles of deep-marine pyroclastic eruptions revealed from axial seamount push core records. *Earth and Planetary Science Letters*, *423*, 219–231. https://doi.org/10.1016/j.epsl.2015.03.043

Preine, J., Crutchley, G., Hübscher, C., Manga, M., Tominaga, M., Beethe, S., et al. (2025). *Data report: Core-seismic integration and time-depth relationships at IODP Expedition 398 Hellenic Arc volcanic field sites* (Vol. 398). Texas A & M University. https://doi.org/10.14379/iodp.proc.398.201.2025

Preine, J., Hübscher, C., Karstens, J., & Nomikou, P. (2022a). Volcano-tectonic evolution of the Christiana-Santorini-Kolumbo rift zone. *Tectonics*, *41*(11), e2022TC007524. https://doi.org/10.1029/2022TC007524

Preine, J., Karstens, J., Hübscher, C., Crutchley, G. J., Druitt, T. H., Schmid, F., & Nomikou, P. (2022b). The hidden giant: How a rift pulse triggered a cascade of sector collapses and voluminous secondary mass-transport events in the early evolution of Santorini. *Basin Research*, *34*(4), 1465–1485. https://doi.org/10.1111/bre.12667

Preine, J., Karstens, J., Hübscher, C., Druitt, T., Kutterolf, S., Nomikou, P., et al. (2024). Hazardous explosive eruptions of a recharging multi-cyclic island arc caldera. *Nature Geoscience*, *17*(4), 323–331. https://doi.org/10.1038/s41561-024-01392-7

Revil, A., Grauls, D., & Brévart, O. (2002). Mechanical compaction of sand/clay mixtures. *Journal of Geophysical Research*, *107*(B11), ECV–11. https://doi.org/10.1029/2001JB000318

Rotella, M. D., Wilson, C. J., Barker, S. J., & Wright, I. C. (2013). Highly vesicular pumice generated by buoyant detachment of magma in subaqueous volcanism. *Nature Geoscience*, *6*(2), 129–132. https://doi.org/10.1038/ngeo1709

Saar, M. O., & Manga, M. (1999). Permeability-porosity relationship in vesicular basalts. *Geophysical Research Letters*, *26*(1), 111–114. https://doi.org/10.1029/1998GL900256

Schlanger, S. O., & Douglas, R. G. (1975). The pelagic ooze-chalk-limestone transition and its implications for marine stratigraphy. *Pelagic Sediments: on Land and under the Sea*, 117–148. https://doi.org/10.1002/9781444304855.ch6

Scudder, R. P., Murray, R. W., & Plank, T. (2009). Dispersed ash in deeply buried sediment from the northwest Pacific Ocean: An example from the Izu–Bonin Arc (ODP Site 1149). *Earth and Planetary Science Letters*, *284*(3–4), 639–648. https://doi.org/10.1016/j.epsl.2009.05.037

Shi, Y., & Wang, C.-Y. (1986). Pore pressure generation in sedimentary basins: Overloading versus aquathermal. *Journal of Geophysical Research*, *91*(B2), 2153–2162. https://doi.org/10.1029/JB091iB02p02153

Shimizu, S., Nakaoka, R., Seama, N., Suzuki-Kamata, K., Kaneko, K., Kiyosugi, K., et al. (2024). Submarine pyroclastic deposits from 7.3 ka caldera-forming Kikai-Akahoya eruption. *Journal of Volcanology and Geothermal Research*, *448*, 108017. https://doi.org/10.1016/j.jvolgeores.2024.108017

Sigurdsson, H., Carey, S., Alexandri, M., Vougioukalakis, G., Croff, K., Roman, C., et al. (2006). Marine investigations of Greece's Santorini volcanic field. Eos. *Transactions - American Geophysical Union*, *87*(34), 337–342. https://doi.org/10.1029/2006EO340001

Straub, S., & Schmincke, H. (1998). Evaluating the tephra input into Pacific Ocean sediments: Distribution in space and time. *Geologische Rundschau*, *87*(3), 461–476. https://doi.org/10.1007/s005310050222

Takeuchi, S., Ishige, K., Uesawa, S., & Suwa, Y. (2024). Unsinkable, long-drifting, millimeter-sized pumice of the 2021 eruption of Fukutoku-Oka-no-Ba submarine volcano. *Progress in Earth and Planetary Science*, *11*(1), 47. https://doi.org/10.1186/s40645-024-00652-9

Terzaghi, K., & Peck, R. B. (1948). *Soil mechanics. Engineering Practice*. John Wiley and Sons, Inc.

Underwood, M. B., Saito, S., & Kubo, Y. (2010). IODP Expedition 322 drills two sites to document inputs to the nankai trough subduction zone. *Scientific Drilling*, *10*, 14–25. https://doi.org/10.2204/iodp.sd.10.02.2010

Walpole, L. (1966). On bounds for the overall elastic moduli of inhomogeneous systems—I. *Journal of the Mechanics and Physics of Solids*, *14*(3), 151–162. https://doi.org/10.1016/0022-5096(66)90035-4

Ward, S., Fauria, K., Jutzeler, M., Dasent, J., & Wright, V. (2025). Isolated vesicles in submarine pumice: Insights from the 2019 Volcano F eruption. *Kingdom of Tonga*. https://doi.org/10.21203/rs.3.rs-7044087/v1

Weller, J. M. (1959). Compaction of sediments. *AAPG Bulletin*, *43*(2), 273–310. https://doi.org/10.1306/0BDA5C9F-16BD-11D7-8645000102C1865D

Wiemer, G., & Kopf, A. (2017). On the role of volcanic ash deposits as preferential submarine slope failure planes. *Landslides*, *14*(1), 223–232. https://doi.org/10.1007/s10346-016-0706-6

Wright, V., & Manga, M. (2025). Rock physics modeling scripts for contrasting seismic velocity and compaction of marine carbonate oozes and volcaniclastic deposits in the South Aegean Volcanic arc. (Version 1.0) [Software]. *Zenodo*. https://doi.org/10.5281/zenodo.15857527

Wulf, S., Keller, J., Satow, C., Gertisser, R., Kraml, M., Grant, K. M., et al. (2020). Advancing Santorini's tephrostratigraphy: New glass geochemical data and improved marine-terrestrial tephra correlations for the past 360 kyrs. *Earth-Science Reviews*, *200*, 102964. https://doi.org/10.1016/j.earscirev.2019.102964